Frequency and Voltage-Constrained MILP Formulation for Power System Restoration Planning

Amir Reza Nikzad and John W. Simpson-Porco

***Abstract*—Black-start power system restoration requires sequentially energizing network elements under low-inertia conditions, where each switching action can drive the system frequency or bus voltages outside safe limits before control systems respond. This paper presents a mixed-integer linear program (MILP) for restoration planning that enforces frequency nadir and voltage constraints. The frequency nadir constraint is based on the average-system-frequency (ASF) model with an IEEEG1 governor-turbine representation, extended to incorporate energy storage system frequency support as a decision variable. Case studies using both MATLAB and PSS/E are presented for a modified IEEE 39-bus test system, demonstrating that the method synthesizes restoration plans which leverage energy storage support while respecting dynamic frequency and voltage limits.**

***Index Terms*—Black-start restoration, energy storage, frequency nadir, MILP, power system restoration.**

I. Introduction

Power system restoration following a wide-area blackout requires sequentially energizing buses, lines, generators, and loads from a designated black-start unit (BSU) under conditions of low inertia and weak voltage support [1], [2]. A single poorly timed switching action can trigger protection devices and undo hours of recovery work [3], and thus effective restoration planning is of critical importance.

Restoration planning formulations based on MILPs have proven effective for jointly optimizing generator start-up sequences, transmission path energization, and load pickup [4]–[6]. The growing penetration of renewable energy has further motivated restoration frameworks incorporating wind and storage resources [7], with low inertia and frequency regulation identified as the central open challenges [8].

During restoration, each load pickup or generator cranking event produces a power imbalance, which can reduce the frequency below safe limits before turbine-governor systems respond. This and other dynamic phenomena can trigger protection devices and halt restoration [9]. Current industry practice relies on rule-of thumb constraints that limit per-step load pickup based on available online generation capacity, but do not attempt to capture and account for the true dynamic security margins of the system [10].

Frequency nadir constraints have been developed in the related context of unit commitment under high renewable penetration [11], [12], but assume stable inertia and fixed topology — conditions that do not hold during restoration, where inertia evolves and topology changes at every step. Existing restoration MILP formulations address generator start-up sequencing and line re-energizing without dynamic security constraints [13]. Frequency regulation has been incorporated into restoration planning for high-renewable systems [14], but without considering voltage bounds or energy storage support.

Contributions: In [15], [16] the authors developed a frequency nadir-constrained MILP restoration planning methodology. The method incorporated participation from energy storage, and was validated on a 9-bus test system. The present paper extends these developments and has two main contributions. First, we extend the formulation of [15], [16] by incorporating steady-state voltage and reactive power constraints. These constraints are jointly enforced with the previous frequency constraints, leading to frequency and voltage secure restoration plans. Second, we expand the scale of validation and test the method on a modified IEEE 39-bus test system. Two case studies with PSS/E validation are presented which illustrate how the proposed method synthesizes frequency and voltage-secure restoration plans, balancing safety against speed of restoration, and highlighting the important role energy storage can play in restoration.

II. MILP Restoration Planning Formulation

This section develops the MILP constraints that govern network element switching, generator start-up, storage operation, and power flow during black-start restoration of a single subsystem. This extends [15], [16] to include linearized AC power flow with voltage and reactive power constraints..

Consider a power network with N_{b} buses, N_{l} lines, N_{g} generators, N_{d} loads, and N_{s} storage units over time steps $t \in \{1, \dots, N_t\}$ of uniform duration t_a minutes. The BSU serves as the slack bus with fixed voltage magnitude $V_{\mathrm{bsu},t} = V^{\mathrm{ref}}$ and zero angle $\theta_{\mathrm{bsu},t} = 0$ for all timesteps. At $t = 0$, only the BSU and its bus are active. Element-to-bus adjacency matrices $\mathrm{A}_x \in \{0,1\}^{N_{\mathrm{b}} \times N_x}$, for $x \in \{\mathrm{l}, \mathrm{g}, \mathrm{d}, \mathrm{s}\}$, encode connectivity with $[\mathrm{A}_x]_{i,j} = 1$ if element j of type x is connected to bus i. We let $\mathrm{A}_x^{(i)}$ denote the i-th column of A_x, and $\mathrm{A}_x^\top$ denote its transpose. The signed bus-branch incidence matrix $\mathrm{A} \in \{-1, 0, 1\}^{N_{\mathrm{b}} \times N_{\mathrm{l}}}$ defines network topology and line flow orientations. Each line j has an assigned positive flow direction from a designated from-bus to a designated to-bus; accordingly $[\mathrm{A}]_{i,j} = 1$ if bus i is the from-bus of line j, $[\mathrm{A}]_{i,j} = -1$ if it is the to-bus, and $[\mathrm{A}]_{i,j} = 0$ otherwise.

A binary vector $\boldsymbol{b}_{\mathrm{x},t} \in \{0,1\}^{N_{\mathrm{x}}}$ indicates whether each element of type x is energized at step t, with $b^i_{\mathrm{x},t}$ denoting the i-th entry of $\boldsymbol{b}_{\mathrm{x},t}$. $\boldsymbol{b}_{\mathrm{x}} = \left[\, \boldsymbol{b}_{\mathrm{x},1} \;\cdots\; \boldsymbol{b}_{\mathrm{x},N_{\mathrm{t}}} \,\right]$ collects all values over time,

A. R. Nikzad and J. W. Simpson-Porco are with the Department of Electrical and Computer Engineering, University of Toronto, Canada. (Email: amirreza.nikzad@utoronto.ca; jw.simpson@utoronto.ca)

Research supported by Hydro One Networks Inc. and NSERC ALLRP 597475-2024 “Planning Restoration of Inverter-Based Grids”.

and let $\tilde{\boldsymbol{b}}_{\mathrm{x}} \triangleq \mathbf{1}_{N_{\mathrm{x}} \times N_t} - \boldsymbol{b}_{\mathrm{x}}$ denote the binary complement. For any time-varying vector $\boldsymbol{v}_t$, we define the one-step difference $\Delta \boldsymbol{v}_t \triangleq \boldsymbol{v}_t - \boldsymbol{v}_{t-1}$. As additional notation throughout: bold symbols denote time-varying variable vectors, and non-bold symbols denote fixed parameters. We let $\hat{\boldsymbol{x}}$ be the diagonal matrix formed from a vector $\boldsymbol{x}$, and $M > 0$ is a big-M constant used to relax constraints on de-energized elements. If $\mathsf{pf}_i \in [0,1]$ is a power factor, $\kappa_i \triangleq \tan(\cos^{-1}(\mathsf{pf}_i))$ is the reactive-to-active power ratio of element i.

A. Network Element Constraints

Each network element, once energized, cannot be de-energized during the restoration process (1), and at most one bus, line, or generator may be switched on per step (2).

$$\Delta \boldsymbol{b}_{\mathrm{x},t} \geq \mathbf{0}, \quad \mathrm{x} \in \{\mathrm{b}, \mathrm{l}, \mathrm{g}, \mathrm{d}, \mathrm{s}\}. \tag{1}$$

$$\sum\nolimits_{\mathrm{x} \in \{\mathrm{b},\mathrm{l},\mathrm{g}\}} \mathbf{1}^\top \Delta \boldsymbol{b}_{\mathrm{x},t} \leq 1. \tag{2}$$

where $\mathbf{1} = (1, \ldots, 1)^\top$. Let $\boldsymbol{\theta}_t, \boldsymbol{V}_t \in \mathbb{R}^{N_{\mathrm{b}}}$ denote vectors of bus voltage angles and magnitudes at step t, which satisfy

$$-M \boldsymbol{b}_{\mathrm{b},t} \leq \boldsymbol{\theta}_t \leq M \boldsymbol{b}_{\mathrm{b},t}, \tag{3a}$$

$$\underline{V} \boldsymbol{b}_{\mathrm{b},t} \leq \boldsymbol{V}_t \leq \overline{V} \boldsymbol{b}_{\mathrm{b},t}, \tag{3b}$$

where $\underline{V}$ and $\overline{V}$ are uniform lower and upper magnitude bounds. Note that when a bus is not energized, the corresponding element of $\boldsymbol{b}_{\mathrm{b},t}$ equals zero, forcing the corresponding angle and voltage to zero.

The connectivity constraints in (4) ensure the energized subgraph remains connected. A line carries power only if both endpoint buses are energized (4a); a newly energized bus must connect to at least one existing energized line (4b); lines and loads may only be energized if their host bus was already energized in the preceding step (4c); and all elements connect only to currently energized buses (4d).

$$\mathrm{A}_{\mathrm{l}}^{(i)} \boldsymbol{b}_{\mathrm{l},t}^i \leq \boldsymbol{b}_{\mathrm{b},t}, \quad i \in \{1, \ldots, N_{\mathrm{l}}\}, \tag{4a}$$

$$\mathrm{A}_{\mathrm{l}} \boldsymbol{b}_{\mathrm{l},t} \geq \boldsymbol{b}_{\mathrm{b},t} - \boldsymbol{b}_{\mathrm{b},0}, \tag{4b}$$

$$\mathrm{A}_{\mathrm{x}}^\top \boldsymbol{b}_{\mathrm{b},t-1} \geq \boldsymbol{b}_{\mathrm{x},t}, \quad x \in \{\mathrm{l}, \mathrm{d}\}, \tag{4c}$$

$$\mathrm{A}_{\mathrm{x}} \boldsymbol{b}_{\mathrm{x},t} \leq \boldsymbol{b}_{\mathrm{b},t}, \quad x \in \{\mathrm{d}, \mathrm{s}, \mathrm{g}\}. \tag{4d}$$

B. Generator State and Power Constraints

When energized, the ith non-black-start unit (NBSU) passes through three sequential states: (i) cranking for t_{c}^i steps, during which generator i draws auxiliary power P_{c}^i from the network, (ii) ramping for t_{r}^i steps, during which its output rises at rate r^i per step, and (iii) online, under normal dispatch. Note that $b_{\mathrm{g},t}^i$ equals one if generator i is energized at time t (i.e., cranking, ramping, or online), and equals zero otherwise. Binary variables $b_{\mathrm{gc},t}^i$, $b_{\mathrm{gr},t}^i$, and $b_{\mathrm{go},t}^i$ indicate the cranking, ramping, or online states at step t, respectively; these are uniquely determined from the energization history via

$$b_{\mathrm{gc},t}^i = b_{\mathrm{g},t}^i - b_{\mathrm{g},t-t_{\mathrm{c}}^i}^i, \tag{5a}$$

$$b_{\mathrm{gr},t}^i = b_{\mathrm{g},t-t_{\mathrm{c}}^i}^i - b_{\mathrm{g},t-t_{\mathrm{c}}^i-t_{\mathrm{r}}^i}^i, \tag{5b}$$

$$b_{\mathrm{go},t}^i = b_{\mathrm{g},t}^i - b_{\mathrm{gc},t}^i - b_{\mathrm{gr},t}^i. \tag{5c}$$

During cranking, active power is fixed at $-\boldsymbol{P}_{\mathrm{c}}$, and during ramping, active power tracks a monotonically increasing reference $\boldsymbol{P}_{\mathrm{r},t}$, each component of which rises at rate r^i per step. These constraints are written as

$$-M \tilde{\boldsymbol{b}}_{\mathrm{gc},t} \leq \boldsymbol{P}_{\mathrm{g},t} + \boldsymbol{P}_{\mathrm{c}} \leq M \tilde{\boldsymbol{b}}_{\mathrm{gc},t}, \tag{6a}$$

$$-M \tilde{\boldsymbol{b}}_{\mathrm{gr},t} \leq \boldsymbol{P}_{\mathrm{g},t} - \boldsymbol{P}_{\mathrm{r},t} \leq M \tilde{\boldsymbol{b}}_{\mathrm{gr},t}, \tag{6b}$$

$$-M \boldsymbol{b}_{\mathrm{gr},t} \leq \boldsymbol{P}_{\mathrm{r},t} \leq M \boldsymbol{b}_{\mathrm{gr},t}, \tag{6c}$$

$$-M \tilde{\boldsymbol{b}}_{\mathrm{gr},t} \leq \Delta \boldsymbol{P}_{\mathrm{r},t} - \boldsymbol{r} \leq M \tilde{\boldsymbol{b}}_{\mathrm{gr},t}. \tag{6d}$$

Once online, active power is bounded by per-generator limits $\underline{P}_{\mathrm{g}}^i$ and $\overline{P}_{\mathrm{g}}^i$, with ramp-rate limits, via (7). The pre-online indicator $\boldsymbol{\Phi}_t \triangleq \boldsymbol{b}_{\mathrm{gc},t} + \boldsymbol{b}_{\mathrm{gr},t}$ relaxes the active power bounds during cranking and ramping, where active power is already constrained by (6). The post-cranking indicator $\boldsymbol{\Psi}_t \triangleq \boldsymbol{b}_{\mathrm{gr},t} + \boldsymbol{b}_{\mathrm{go},t}$ equals one when the generator is ramping or online; reactive power is zero outside this window and bounded by $\underline{Q}_{\mathrm{g}}^i$ and $\overline{Q}_{\mathrm{g}}^i$ within it, as enforced by (7c).

$$\hat{\underline{P}}_{\mathrm{g}} \boldsymbol{b}_{\mathrm{go},t} - M \boldsymbol{\Phi}_t \leq \boldsymbol{P}_{\mathrm{g},t} \leq \hat{\overline{P}}_{\mathrm{g}} \boldsymbol{b}_{\mathrm{go},t} + M \boldsymbol{\Phi}_t, \tag{7a}$$

$$-\boldsymbol{r} - M \tilde{\boldsymbol{b}}_{\mathrm{go},t} \leq \Delta \boldsymbol{P}_{\mathrm{g},t} \leq \boldsymbol{r} + M \tilde{\boldsymbol{b}}_{\mathrm{go},t}, \tag{7b}$$

$$\hat{\underline{Q}}_{\mathrm{g}} \boldsymbol{\Psi}_t \leq \boldsymbol{Q}_{\mathrm{g},t} \leq \hat{\overline{Q}}_{\mathrm{g}} \boldsymbol{\Psi}_t. \tag{7c}$$

To achieve coordinated reactive power sharing among online NBSUs, a voltage–reactive power droop is imposed via (8). The terminal voltage decreases linearly with reactive output according to a generator-specific droop coefficient and a reference voltage V_{ref}. The BSU is excluded since its terminal voltage is assumed fixed.

$$-M \tilde{\boldsymbol{\Psi}}_t \leq \mathrm{A}_{\mathrm{g}}^\top \boldsymbol{V}_t - V_{\mathrm{ref}} \mathbf{1} + \hat{K}_{\mathrm{qv}} \boldsymbol{Q}_{\mathrm{g},t} \leq M \tilde{\boldsymbol{\Psi}}_t, \tag{8}$$

where $\hat{K}_{\mathrm{qv}}$ is the diagonal matrix of droop coefficients.

C. Energy Storage System Constraints

The active power injected by the storage at the grid side is

$$\boldsymbol{P}_{\mathrm{s},t} = \hat{\eta}_{\mathrm{con}} \boldsymbol{P}_{\mathrm{s},t}^{\mathrm{out}} - \hat{\eta}_{\mathrm{con}}^{-1} \boldsymbol{P}_{\mathrm{s},t}^{\mathrm{in}}, \tag{9}$$

where $\boldsymbol{P}_{\mathrm{s},t}^{\mathrm{out}}, \boldsymbol{P}_{\mathrm{s},t}^{\mathrm{in}} \in \mathbb{R}^{N_{\mathrm{s}}}$ are the nonnegative discharge and charge power vectors respectively, and η_{con} denotes the converter efficiency. The stored energy $\boldsymbol{E}_{\mathrm{s},t}$, with initial value $\boldsymbol{E}_{\mathrm{s},0} \in \mathbb{R}^{N_{\mathrm{s}}}$, must remain within the rated energy capacity $\overline{E}_{\mathrm{s}} \in \mathbb{R}^{N_{\mathrm{s}}}$ and evolves according to (10) [17].

$$\mathbf{0} \leq \boldsymbol{E}_{\mathrm{s},t} \leq \overline{E}_{\mathrm{s}}, \tag{10a}$$

$$\boldsymbol{E}_{\mathrm{s},t} = \boldsymbol{E}_{\mathrm{s},t-1} + \tfrac{t_a}{60} \left(\hat{\eta}_{\mathrm{s}} \boldsymbol{P}_{\mathrm{s},t}^{\mathrm{in}} - \hat{\eta}_{\mathrm{s}}^{-1} \boldsymbol{P}_{\mathrm{s},t}^{\mathrm{out}} \right), \tag{10b}$$

where η_{s} is the storage efficiency. Binary variables $\boldsymbol{b}_{\mathrm{s},t}^{\mathrm{in}}, \boldsymbol{b}_{\mathrm{s},t}^{\mathrm{out}} \in \{0,1\}^{N_{\mathrm{s}}}$ indicate active charging and discharging states at step t. In (11a), charge and discharge powers are bounded by the rated power $\overline{P}_{\mathrm{s}} \in \mathbb{R}^{N_{\mathrm{s}}}$ and binary mode indicators $\boldsymbol{b}_{\mathrm{s},t}^{\mathrm{in}}$ and $\boldsymbol{b}_{\mathrm{s},t}^{\mathrm{out}}$. Constraint (11b) prevents simultaneous charging and discharging while requiring bus energization for storage operation.

$$\mathbf{0} \leq \boldsymbol{P}_{\mathrm{s},t}^{\mathrm{in}} \leq \hat{\overline{P}}_{\mathrm{s}} \boldsymbol{b}_{\mathrm{s},t}^{\mathrm{in}}, \quad \mathbf{0} \leq \boldsymbol{P}_{\mathrm{s},t}^{\mathrm{out}} \leq \hat{\overline{P}}_{\mathrm{s}} \boldsymbol{b}_{\mathrm{s},t}^{\mathrm{out}}, \tag{11a}$$

$$\boldsymbol{b}_{\mathrm{s},t}^{\mathrm{in}} + \boldsymbol{b}_{\mathrm{s},t}^{\mathrm{out}} \leq \boldsymbol{b}_{\mathrm{s},t}. \tag{11b}$$

The rate of change of net storage power is bounded by

$$-r_{\mathrm{s}} \le \Delta \boldsymbol{P}_{\mathrm{s},t} \le r_{\mathrm{s}}, \tag{12}$$

where $r_{\mathrm{s}} \in \mathbb{R}^{N_{\mathrm{s}}}$ encodes the ramp rates. Each storage unit operates at a fixed inverter power factor pf^{s} [18], i.e.,

$$\boldsymbol{Q}_{\mathrm{s},t} = \hat{\kappa}^{\mathrm{s}} \boldsymbol{P}_{\mathrm{s},t}. \tag{13}$$

D. Shunt Reactive Power

Transmission lines have shunt capacitances that inject reactive power, and buses may have shunt elements like capacitor banks or reactors. After linearization around nominal voltage, the injection is proportional to the bus voltage and is given by $\boldsymbol{Q}^{\mathrm{sh}} \approx \hat{B}^{\mathrm{sh}}(2\boldsymbol{V}_t - \mathbf{1})$ for energized elements.

Let $\mathrm{A}_{\mathrm{lf}}, \mathrm{A}_{\mathrm{lt}} \in \{0,1\}^{N_{\mathrm{b}} \times N_{\mathrm{l}}}$ denote the from-bus and to-bus sub-matrices of A_{l}, where $[\mathrm{A}_{\mathrm{lf}}]_{i,j} = 1$ if bus i is the from-bus of line j, and similarly for A_{lt}. The line charging susceptance matrix $\hat{B}^{\mathrm{sh}}_{\mathrm{l}}$ is the diagonal matrix of total line charging susceptances, split equally between the two ends. The shunt injections at the from and to ends of each line, $\boldsymbol{Q}^{\mathrm{sh,f}}_{\mathrm{l},t}$ and $\boldsymbol{Q}^{\mathrm{sh,t}}_{\mathrm{l},t}$, are zeroed on de-energized lines and set by the shunt formula on energized ones via (14).

$$-M\boldsymbol{b}_{\mathrm{l},t} \le \boldsymbol{Q}^{\mathrm{sh,f}}_{\mathrm{l},t} \le M\boldsymbol{b}_{\mathrm{l},t}, \tag{14a}$$
$$-M\tilde{\boldsymbol{b}}_{\mathrm{l},t} \le \boldsymbol{Q}^{\mathrm{sh,f}}_{\mathrm{l},t} - \tfrac{1}{2}\hat{B}^{\mathrm{sh}}_{\mathrm{l}}(2\mathrm{A}^{\top}_{\mathrm{lf}}\boldsymbol{V}_t - \mathbf{1}) \le M\tilde{\boldsymbol{b}}_{\mathrm{l},t}, \tag{14b}$$
$$-M\boldsymbol{b}_{\mathrm{l},t} \le \boldsymbol{Q}^{\mathrm{sh,t}}_{\mathrm{l},t} \le M\boldsymbol{b}_{\mathrm{l},t}, \tag{14c}$$
$$-M\tilde{\boldsymbol{b}}_{\mathrm{l},t} \le \boldsymbol{Q}^{\mathrm{sh,t}}_{\mathrm{l},t} - \tfrac{1}{2}\hat{B}^{\mathrm{sh}}_{\mathrm{l}}(2\mathrm{A}^{\top}_{\mathrm{lt}}\boldsymbol{V}_t - \mathbf{1}) \le M\tilde{\boldsymbol{b}}_{\mathrm{l},t}. \tag{14d}$$

A similar formula applies to bus shunt elements via (15), where $\hat{B}^{\mathrm{sh}}_{\mathrm{b}}$ is the diagonal matrix of bus shunt susceptances, with $B^{\mathrm{sh}}_{\mathrm{b},i} > 0$ for capacitive elements and $B^{\mathrm{sh}}_{\mathrm{b},i} < 0$ for inductive elements, and $\boldsymbol{Q}^{\mathrm{sh,b}}_{\mathrm{b},t}$ is the resulting reactive injection at each bus.

$$-M\boldsymbol{b}_{\mathrm{b},t} \le \boldsymbol{Q}^{\mathrm{sh,r}}_{\mathrm{b},t} \le M\boldsymbol{b}_{\mathrm{b},t}, \tag{15a}$$
$$-M\tilde{\boldsymbol{b}}_{\mathrm{b},t} \le \boldsymbol{Q}^{\mathrm{sh,r}}_{\mathrm{b},t} - \hat{B}^{\mathrm{sh}}_{\mathrm{b}}(2\boldsymbol{V}_t - \mathbf{1}) \le M\tilde{\boldsymbol{b}}_{\mathrm{b},t}. \tag{15b}$$

The total shunt reactive injection at each bus aggregates contributions from both ends of connected lines and any local reactor via (16).

$$\boldsymbol{Q}^{\mathrm{sh}}_{\mathrm{b},t} = \mathrm{A}_{\mathrm{lf}}\boldsymbol{Q}^{\mathrm{sh,f}}_{\mathrm{l},t} + \mathrm{A}_{\mathrm{lt}}\boldsymbol{Q}^{\mathrm{sh,t}}_{\mathrm{l},t} + \boldsymbol{Q}^{\mathrm{sh,b}}_{\mathrm{b},t}. \tag{16}$$

E. Power Balance and Flow Constraints

Nodal active and reactive power balance is enforced at every bus via (17), where $\hat{P}_{\mathrm{d}}$ and $\hat{Q}_{\mathrm{d}}$ represent diagonal matrices of active and reactive demands, and $\boldsymbol{Q}_{\mathrm{s},t}$ is the storage reactive power defined in (13).

$$\mathrm{A}\boldsymbol{P}_{\mathrm{l},t} = \mathrm{A}_{\mathrm{g}}\boldsymbol{P}_{\mathrm{g},t} - \mathrm{A}_{\mathrm{d}}\hat{P}_{\mathrm{d}}\boldsymbol{b}_{\mathrm{d},t} + \mathrm{A}_{\mathrm{s}}\boldsymbol{P}_{\mathrm{s},t}, \tag{17a}$$
$$\mathrm{A}\boldsymbol{Q}_{\mathrm{l},t} = \mathrm{A}_{\mathrm{g}}\boldsymbol{Q}_{\mathrm{g},t} - \mathrm{A}_{\mathrm{d}}\hat{Q}_{\mathrm{d}}\boldsymbol{b}_{\mathrm{d},t} + \mathrm{A}_{\mathrm{s}}\boldsymbol{Q}_{\mathrm{s},t} + \boldsymbol{Q}^{\mathrm{sh}}_{\mathrm{b},t}. \tag{17b}$$

The AC line flow equations are linearized via a first-order Taylor expansion around the flat operating point ($V = 1$ p.u., $\theta = 0$) [19], [20]. For a line from bus i to bus j with series conductance $G_{ij} > 0$ and susceptance magnitude $B_{ij} > 0$, the linearized flows are

$$P_{ij} = G_{ij}(V_i - V_j) + B_{ij}(\theta_i - \theta_j), \tag{18a}$$
$$Q_{ij} = B_{ij}(V_i - V_j) - G_{ij}(\theta_i - \theta_j). \tag{18b}$$

Stacking these equations for all N_{l} lines into vectors $\boldsymbol{P}_{\mathrm{l},t}, \boldsymbol{Q}_{\mathrm{l},t} \in \mathbb{R}^{N_{\mathrm{l}}}$, and defining $\hat{G}$ and $\hat{B}$ as diagonal matrices in the obvious manner, these equalities are enforced on energized lines and zeroed on de-energized ones via (19).

$$-M\tilde{\boldsymbol{b}}_{\mathrm{l},t} \le \boldsymbol{P}_{\mathrm{l},t} - \hat{G}\mathrm{A}^{\top}\boldsymbol{V}_t - \hat{B}\mathrm{A}^{\top}\boldsymbol{\theta}_t \le M\tilde{\boldsymbol{b}}_{\mathrm{l},t}, \tag{19a}$$
$$-M\boldsymbol{b}_{\mathrm{l},t} \le \boldsymbol{P}_{\mathrm{l},t} \le M\boldsymbol{b}_{\mathrm{l},t}, \tag{19b}$$
$$-M\tilde{\boldsymbol{b}}_{\mathrm{l},t} \le \boldsymbol{Q}_{\mathrm{l},t} - \hat{B}\mathrm{A}^{\top}\boldsymbol{V}_t + \hat{G}\mathrm{A}^{\top}\boldsymbol{\theta}_t \le M\tilde{\boldsymbol{b}}_{\mathrm{l},t}, \tag{19c}$$
$$-M\boldsymbol{b}_{\mathrm{l},t} \le \boldsymbol{Q}_{\mathrm{l},t} \le M\boldsymbol{b}_{\mathrm{l},t}. \tag{19d}$$

F. Apparent Power Limits

Thermal limits on line and generator apparent power, $P^2 + Q^2 \le \overline{S}^2$, are nonlinear and are inner-approximated by a regular N-sided polygon inscribed in the feasible circle [21]. The n-th edge constraint for $n = 1, \ldots, N$ with $\phi_n = 2\pi(n-1)/N$ is applied to lines and generators via

$$\cos\phi_n\, \boldsymbol{P}_{\mathrm{g},t} + \sin\phi_n\, \boldsymbol{Q}_{\mathrm{g},t} \le \hat{\overline{S}}_{\mathrm{g}}\boldsymbol{b}_{\mathrm{g},t}, \tag{20a}$$
$$\cos\phi_n\, \boldsymbol{P}_{\mathrm{l},t} + \sin\phi_n\, \boldsymbol{Q}_{\mathrm{l},t} \le \hat{\overline{S}}_{\mathrm{l}}\boldsymbol{b}_{\mathrm{l},t}, \tag{20b}$$

for $n \in \{1, \ldots, N\}$, where $\hat{\overline{S}}_{\mathrm{g}}$ and $\hat{\overline{S}}_{\mathrm{l}}$ are diagonal matrices of MVA ratings.

III. Power System Restoration Formulation with Dynamic Security Constraints

Restoration actions introduce abrupt power changes that can drive system frequency outside of safe limits before control systems respond. This section describes a linearized frequency constraint which will be embedded directly in the restoration planning MILP.

A. Frequency Security Constraints

When a load is picked up or a NBSU begins cranking, the resulting power imbalance causes the system frequency to drop until the governor response of online generators restores balance. The lowest point of this transient — the frequency nadir — must not fall below $f_0 - |\Delta f_{\mathrm{lim}}|$, where f_0 is the nominal frequency and $|\Delta f_{\mathrm{lim}}|$ is the maximum allowable deviation. The following constraint, derived in full in [16] based on a center-of-inertia frequency model and an IEEEG1-type turbine-governor, ensures the frequency deviation is not exceeded. Define the net electrical power imbalance $\boldsymbol{\Delta P}_{\mathrm{e},t} \in \mathbb{R}$ at step t as

$$\boldsymbol{\Delta P}_{\mathrm{e},t} = \boldsymbol{P}^{\top}_{\mathrm{d}}\Delta\boldsymbol{b}_{\mathrm{d},t} + \boldsymbol{P}^{\top}_{\mathrm{c}}\Delta\boldsymbol{b}_{\mathrm{gc},t}, \tag{21}$$

which accounts for newly picked-up loads and cranking generators drawing power $\boldsymbol{P}_{\mathrm{c}}$. The frequency nadir constraint requires $\boldsymbol{\Delta P}_{\mathrm{e},t}$ to satisfy

$$\boldsymbol{\Delta P}_{\mathrm{e},t} \le \boldsymbol{\Delta P}_{\mathrm{e,max},t} \triangleq \boldsymbol{g}_{0,t} + \boldsymbol{g}^{\top}_{\mathrm{s},t}\Delta\boldsymbol{P}^{\mathrm{ref}}_{\mathrm{s},t}, \tag{22}$$

for all $t \in \{1, \ldots, N_t\}$. Here, $\Delta \boldsymbol{P}^{\text{ref}}_{\text{s},t} \in \mathbb{R}^{N_\text{s}}$ denotes the vector of storage setpoint changes at step t, with positive values indicating net discharge increase. The parameters$\boldsymbol{g}_{0,t}$ and $\boldsymbol{g}_{s,t}$ depend on the system inertia and IEEEG1 governor parameters, which evolve as generators synchronize; see [16] for their derivation and expressions. Note that $\boldsymbol{g}_{0,t}$ is the base limit without storage support, and $\boldsymbol{g}_{s,t}$ is the storage sensitivity vector whose ith entry quantifies the increase in the limit per unit of setpoint change from storage unit i.

B. Complete Restoration Framework

The restoration objective is to maximize the weighted sum of energized elements over the planning horizon, where $\boldsymbol{w}_\text{x}$ is the priority weight vector for element type x, with higher weights assigned to generators and critical loads.

$$\max \; z = \sum_{t \in N_T} \sum_{\text{x} \in \{\text{b,l,g,d}\}} \boldsymbol{w}_\text{x}^\top \boldsymbol{b}_{\text{x},t}, \tag{23}$$

$$\text{s.t.} \quad (1)\text{–}(17),\ (19), (20), (22).$$

The dynamic security parameters in (22) depend nonlinearly on the binary restoration decisions, making (23) an MINLP in general. To recover tractability, a receding-horizon algorithm is adopted: at each iteration ν starting at step t, the generator state binaries are fixed over $\{t+1, \ldots, t+t_\text{h}\}$ using the known durations t_c and t_r, all dynamic security parameters are precomputed from these fixed binaries and the current topology, and the resulting MILP is solved over this window. The first step is then committed to the plan and the horizon advances. The procedure is summarized in Algorithm 1; full details are given in [16].

Algorithm 1: Receding-Horizon Restoration

Input: Window t_h, network data, initial state at $t = 0$, $\nu = 0$
Output: Restoration plan $\{\boldsymbol{b}^*_{\text{x},t}\}$
while $t < N_\text{t}$ **do**
  Fix generator binaries over the lookahead horizon
  Precompute security parameters
  Solve (23) over $\{t+1, \ldots, t+t_\text{h}\}$
  Commit $\boldsymbol{b}^*_{\text{x},t+1}$ to the restoration plan
  $t \leftarrow t+1, \quad \nu \leftarrow \nu+1$
end

IV. Case Study

The proposed framework is validated on a modified IEEE 39-bus test system [22]. The generator at bus 39 is designated as the BSU; all other generators serve as NBSUs. Two storage units are connected at buses 18 and 24, each rated at 50 MWh energy capacity and 20 MW power rating. The system topology and element locations are illustrated in Fig. 1.

The planning horizon is $N_T = 50$ steps of duration $t_a = 2$ min, with receding-horizon lookahead window $t_h = 10$ timesteps. The frequency deviation limit is $|\Delta f_\text{lim}| = 0.5$ Hz, steady-state voltage limits are $[\underline{V}, \overline{V}] = [0.9, 1.1]$ p.u. MILPs are formulated in YALMIP [23] and solved with Gurobi [24]. The resulting restoration plans are validated through two dynamic simulations: a MATLAB ODE simulation of the closed-loop ASF model, and a full PSS/E dynamic simulation that captures transient dynamics and inter-machine interactions beyond the scope of the ASF model. Two test cases are considered, differing only in whether storage support is active.

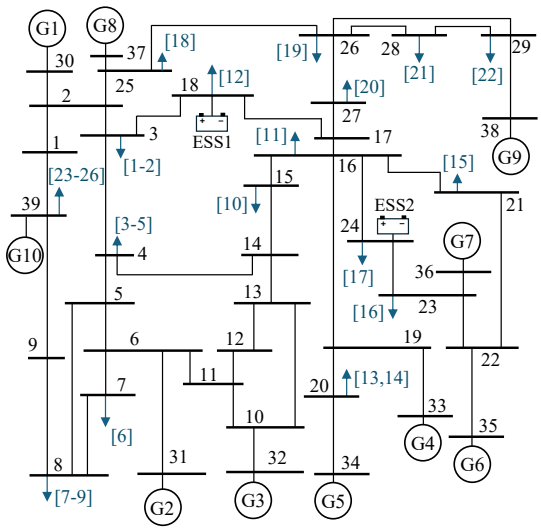

Fig. 1. Modified IEEE 39-bus test system. Load IDs are marked in blue and bus numbers in black.

Without storage ($\Delta \boldsymbol{P}^{\text{ref}}_{s,t} = 0$): The generator energization sequence, center of inertia frequency deviation, and load pickup schedule are shown in Fig. 2. The frequency deviation remains within $|\Delta f_\text{lim}|$. The MATLAB ODE and PSS/E frequency trajectories closely match, confirming the fidelity of the restoration plan under detailed dynamic simulation. Load 24, with a demand exceeding the maximum allowable power imbalance $\boldsymbol{\Delta P}_{\text{e,max,t}}$, cannot be safely energized and is excluded from the restoration plan.

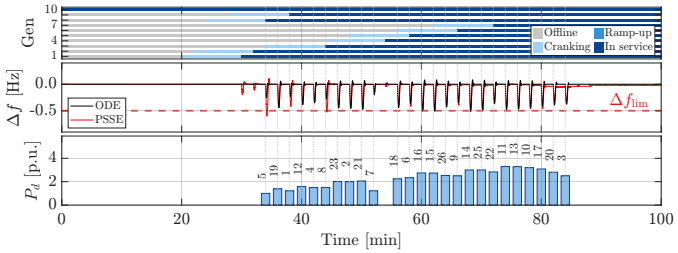

Fig. 2. Without storage: generator energization sequence, center of inertia frequency deviation, and load pickup schedule. Load 24 is not restored.

Proposed framework (with storage): The complete framework is applied with storage support constraints all active. As shown in Fig. 3, all 26 loads are restored and the frequency deviation remains within $|\Delta f_\text{lim}|$ throughout the entire horizon, with MATLAB ODE and PSS/E results in close agreement. When load 24 is picked up, both storage units discharge, reducing the net power imbalance and effectively increasing $\boldsymbol{\Delta P}_{\text{e,max,t}}$ beyond the inertia-alone limit, thereby enabling the restoration of the load without violating the frequency constraint.

The storage charge and discharge profiles are shown in Fig. 4. The storage discharges when large loads are picked

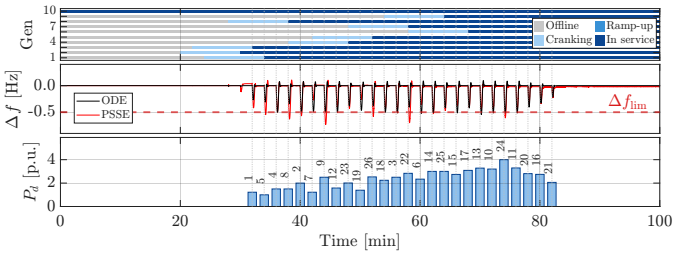

Fig. 3. Proposed framework: generator energization sequence, center of inertia frequency deviation, and load pickup schedule. All 26 loads are restored.

up and charges otherwise.

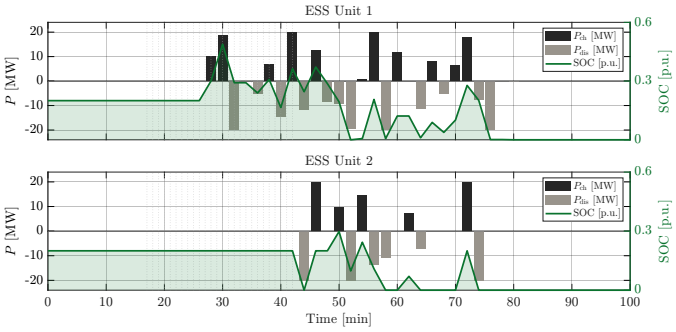

Fig. 4. Storage units active power charge and discharge profiles.

Fig. 5 compares the steady-state bus voltage magnitudes $\boldsymbol{V}_t$ from the MILP and PSS/E for selected buses. The PSS/E voltages shown are the settled values after the AVR has responded at each restoration step. Voltages remain within the prescribed limits throughout the restoration horizon, and the MILP and PSS/E results are in close agreement, with minor discrepancies arising from the linearized power flow and linearized shunt reactive power models.

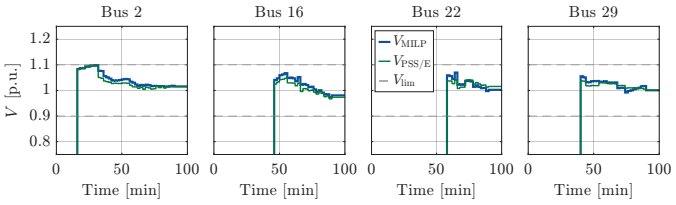

Fig. 5. Bus voltage magnitudes $\boldsymbol{V}_t$ for the MILP and PSS/E for selected buses.

V. Conclusion

This paper proposed a frequency-constrained MILP formulation for black-start power system restoration planning with storage support. Linearized frequency nadir constraints based on the IEEEG1 governor-turbine model along with the linearized AC power flow were embedded in a receding-horizon restoration MILP. Case studies on the modified IEEE 39-bus test system demonstrated that the proposed framework restores all loads within the prescribed frequency and voltage bounds, showing that inertia-aware dynamic security constraints can be successfully integrated into restoration plans.

References

[1] M. Adibi and L. Fink, "Overcoming restoration challenges associated with major power system disturbances - restoration from cascading failures," *IEEE Power Energy Mag.*, vol. 4, no. 5, pp. 68–77, 2006.

[2] F. Qiu and P. Li, "An integrated approach for power system restoration planning," *Proc. IEEE*, vol. 105, no. 7, pp. 1234–1252, 2017.

[3] Y. Liu, R. Fan, and V. Terzija, "Power system restoration: a literature review from 2006 to 2016," *J. Mod. Power Syst. Clean Energy*, vol. 4, no. 3, pp. 332–341, 2016.

[4] W. Sun, C.-C. Liu, and S. Liu, "Black start capability assessment in power system restoration," in *IEEE PES General Meeting*, 2011, pp. 1–7.

[5] G. Patsakis, D. Rajan, I. Aravena, J. Rios, and S. Oren, "Optimal black start allocation for power system restoration," *IEEE Trans. Power Syst.*, vol. 33, no. 6, pp. 6766–6776, 2018.

[6] F. Qiu, J. Wang, C. Chen, and J. Tong, "Optimal black start resource allocation," *IEEE Trans. Power Syst.*, vol. 31, no. 3, pp. 2493–2494, 2016.

[7] A. Golshani, W. Sun, Q. Zhou, Q. P. Zheng, and Y. Hou, "Incorporating wind energy in power system restoration planning," *IEEE Trans. Smart Grid*, vol. 10, no. 1, pp. 16–28, 2019.

[8] K. Liang, H. Wang, D. Pozo, and V. Terzija, "Power system restoration with large renewable penetration: State-of-the-art and future trends," *Int. J. Electr. Power Energy Syst.*, vol. 155, p. 109494, 2024.

[9] J. Vermunicht, T. Škrjanc, B. Sütő, D. Van Hertem, U. Rudež, D. Raisz, and W. Leterme, "Decision support for power system restoration: Mitigating risks of dynamic phenomena," in *IEEE PES ISGT Europe*, 2024, pp. 1–6.

[10] Independent Electricity System Operator (IESO), "Part 7.8: Ontario power system restoration plan," IESO, Toronto, ON, Canada, Tech. Rep., 2022.

[11] X. Liu, X. Fang, N. Gao, H. Yuan, A. Hoke, H. Wu, and J. Tan, "Frequency nadir constrained unit commitment for high renewable penetration island power systems," *IEEE Open Access J. Power Energy*, vol. 11, pp. 141–153, 2024.

[12] Z. Zhang, E. Du, F. Teng, N. Zhang, and C. Kang, "Modeling frequency dynamics in unit commitment with a high share of renewable energy," *IEEE Trans. Power Syst.*, vol. 35, no. 6, pp. 4383–4395, 2020.

[13] Y. Xie, D. Li, Y. Xu, Q. Wu, and M. Yin, "A milp-based restoration planning method for generator start-up considering flexible re-energizing times of transmission lines," *Int. J. Electr. Power Energy Syst.*, vol. 124, p. 106357, 2021.

[14] C. Yang, H. Liao, S. Wang, Y. Bai, S. Li, and J. Zhao, "Coordinated restoration of generators and load for the high renewable energy penetrated power system with frequency regulation," in *2023 IEEE 7th Conf. on Energy Internet and Energy Syst. Integr. (EI2)*, 2023, pp. 5213–5217.

[15] X. Zou, I. Farhat, and J. W. Simpson-Porco, "A method for incorporating frequency nadir limits in power system restoration planning," in *2025 IEEE Electrical Power and Energy Conference (EPEC)*, 2025, pp. 254–259.

[16] X. Zou, A. R. Nikzad, I. Farhat, and J. W. Simpson-Porco, "Frequency nadir-constrained power system restoration planning with energy storage," 2026. [Online]. Available: https://arxiv.org/abs/2605.14099

[17] J. M. Miller, H. N. V. Pico, I. Dobson, A. Bernstein, and B. Cui, "Feedback control approaches for restoration of power grids from blackouts," *Electric Power Systems Research*, vol. 211, p. 108414, 2022.

[18] S. Karagiannopoulos, P. Aristidou, and G. Hug, "Co-optimisation of planning and operation for active distribution grids," in *2017 IEEE Manchester PowerTech*, 2017, pp. 1–6.

[19] J. Yang, N. Zhang, C. Kang, and Q. Xia, "A state-independent linear power flow model with accurate estimation of voltage magnitude," *IEEE Trans. Power Syst.*, vol. 32, no. 5, pp. 3607–3617, 2017.

[20] Z. Yang, K. Xie, J. Yu, H. Zhong, N. Zhang, and Q. Xia, "A general formulation of linear power flow models: Basic theory and error analysis," *IEEE Trans. Power Syst.*, vol. 34, no. 2, pp. 1315–1324, 2019.

[21] R. S. Ferreira, C. L. T. Borges, and M. V. F. Pereira, "A flexible mixed-integer linear programming approach to the ac optimal power flow in distribution systems," *IEEE Trans. Power Syst.*, vol. 29, no. 5, pp. 2447–2459, 2014.

[22] Texas A&M University, "Electric grid test cases," https://electricgrids.engr.tamu.edu/electric-grid-test-cases/.

[23] J. Löfberg, "Yalmip : A toolbox for modeling and optimization in matlab," in *In Proceedings of the CACSD Conference*, Taipei, Taiwan, 2004.

[24] Gurobi Optimization, LLC, "Gurobi Optimizer Reference Manual," 2026. [Online]. Available: https://www.gurobi.com